Assessing pupil size as an index of activation of subcortical ascending arousal system nuclei during rest

Beth Lloyd[1], Lycia D. de Voogd[2,3], Verónica Mäki-Marttunen[1], Sander Nieuwenhuis[1]

[1] Institute of Psychology, Leiden University, Leiden, Netherlands

[2] Donders Institute, Centre for Cognitive Neuroimaging, Radboud University, Nijmegen, The Netherlands.

[3] Behavioural Science Institute, Radboud University Nijmegen, The Netherlands.

Corresponding author:

Beth Lloyd

Email address: b.lloyd@fsw.leidenuniv.nl

Address: Wassenaarseweg 52, 2333 AK Leiden

Abstract

Neuromodulatory nuclei that are part of the ascending arousal system (AAS) play a crucial role in regulating cortical state and optimizing task performance. Pupil diameter, under constant luminance conditions, is increasingly used as an index of activity of these AAS nuclei. Indeed, task-based functional imaging studies in humans have begun to provide evidence of stimulus-driven pupil-AAS coupling. However, whether there is such a tight pupil-AAS coupling during rest is not clear. To address this question, we examined simultaneously acquired resting-state fMRI and pupil-size data from 74 participants, focusing on six AAS nuclei: the locus coeruleus, ventral tegmental area, substantia nigra, dorsal and median raphe nuclei, and cholinergic basal forebrain. Activation in all six AAS nuclei was optimally correlated with pupil size at 0- to 2-second lags, suggesting that spontaneous pupil changes were almost immediately followed by corresponding BOLD-signal changes in the AAS. These results suggest that spontaneous changes in pupil size that occur during states of rest can be used as a noninvasive general index of activity in AAS nuclei. Importantly, the nature of pupil-AAS coupling during rest appears to be vastly different from the relatively slow canonical hemodynamic response function that has been used to characterize task-related pupil-AAS coupling.

Keywords

Resting-state fMRI; pupillometry; subcortex; locus coeruleus; arousal; hemodynamic response

Introduction

Neuromodulatory brainstem, midbrain, and basal forebrain nuclei that together form the core of the ascending arousal system (AAS) are situated deep in the brain. They have widespread projections to the cortex, making them ideally suited to alter cortical states and optimize task performance (Bunzeck & Düzel, 2006; de Gee et al., 2017; Shine et al., 2021; Thiele & Bellgrove, 2018). Pupil diameter, under constant luminance conditions, has vastly been used as a proxy for activity of these subcortical nuclei (Joshi & Gold, 2020). Indeed, task-related activity of these nuclei is accompanied by changes in pupil size and its first-order derivative (i.e., rate of change), as evidenced by animal studies and functional magnetic resonance imaging (fMRI) studies in humans (Cazettes et al., 2021; de Gee et al., 2017; Murphy et al., 2014; Varazzani et al., 2015; Yang et al., 2021). Animal studies have also found pupil-AAS coupling of spontaneous fluctuations during rest (Joshi et al., 2016; Reimer et al., 2016). However, it is still largely unclear whether similar coupling can be found between resting-state fluctuations of pupil size and blood oxygen level-dependent (BOLD) signals in the human AAS. Assessing if and how activity in neuromodulatory brainstem, midbrain, and basal forebrain nuclei can be inferred from pupil size measurements is relevant for promoting our scientific and clinical understanding of AAS function.

A small number of human resting-state fMRI studies have investigated the brain activity associated with fluctuations in pupil size (Breeden et al., 2016; Mäki-Marttunen & Espeseth, 2021; Murphy et al., 2014; Yellin et al., 2015) and pupil derivative (DiNuzzo et al., 2019; Schneider et al., 2016). Their results with respect to a coupling between pupil size and AAS activity are inconclusive, with most studies not reporting evidence for such a relationship. However, the majority of these studies did not focus on the AAS, Moreover, they did not include specific localization methods to delineate AAS regions-of-interest (ROIs) or correct for physiological sources of noise, such as cardiac and respiratory fluctuations. These approaches are important for reliable measurements in these subcortical nuclei (Brooks et al., 2013; Matt et al., 2019). To date, only Murphy et al. (2014) specifically investigated the relationship between pupil size and one AAS nucleus, namely the locus coeruleus (LC). The authors found a positive coupling between fluctuations in pupil size and activation in the LC during rest. To our knowledge, there have been no human fMRI studies so far that have reported a relationship between pupil size and other AAS nuclei during rest, despite the growing evidence from animal studies (Joshi et al., 2016; Reimer et al., 2016) speaking for such a relationship. Therefore, in the current study, we aimed to investigate whether pupil size (and the pupil derivative) can be used as an index of activity in neuromodulatory AAS nuclei during rest.

To address this aim, we systematically examined simultaneous measurements of resting-state fMRI and pupil size from a large sample of healthy adults (N=74). We monitored BOLD signal from a number of subcortical nuclei part of the AAS and implicated in the control of cortical arousal levels: the LC, the ventral tegmental area (VTA), dopaminergic substantia nigra (SN), the dorsal (DR) and median (MR) raphe nuclei and the nucleus basalis of Meynert in the cholinergic basal forebrain (BF). Due to their size and location in the brain, studying these small nuclei using fMRI comes with a unique set of challenges (Forstmann et al., 2017; Liu et al., 2017a; Matt et al., 2019). Here, we mitigated these challenges by implementing a number of methods, including multi-echo imaging to increase signal-to-noise ratio in subcortical structures (Miletić et al., 2020; Puckett et al., 2018; Turker et al., 2021), neuromelanin-weighted T1 imaging for delineation of the LC (Clewett et al., 2016; Keren et al., 2015; Mäki-

Marttunen & Espeseth, 2021; Priovoulos et al., 2018), optimized brainstem co-registration (ANTs SyN; Ewert et al., 2019), physiological noise regression to suppress respiratory and cardiac artifacts (Glover et al., 2000; Harvey et al., 2008), and no spatial smoothing of fMRI data (de Gee et al., 2017).

As a first analysis, we intended to reproduce the analyses from two previous studies that did (Murphy et al., 2014) and did not (Schneider et al., 2016) find AAS correlates of pupil size during rest. The analyses in these studies were performed under the assumption that the relationship between pupil size and resting-state BOLD activity in AAS nuclei is governed by the canonical hemodynamic response function (HRF). As we could not replicate previous findings, we reasoned it is possible that during rest, when there is no external stimulus driving neural activity, the temporal relation between pupil dilation and AAS activity does not follow an HRF-like waveform. Therefore, we began examining the temporal relationship between pupil time series and AAS-BOLD activation using various transfer functions based on the canonical HRF, taking into account that subcortical structures have been characterized by faster time-to-peak (TTP) of the HRF than the cortex (Lau et al., 2011; Lewis et al., 2018; Yen et al., 2011). It is possible that the HRF does not provide an adequate model of the relationship between resting-state fluctuations in pupil size and AAS BOLD activity. We therefore also explored cross-correlations between AAS BOLD activity and the unconvolved pupil time series, systematically varying the forward and backward lag between the two measures. Together, these analyses offer new insights into the use of pupil size as an index of activity in AAS regions.

Results

The Results section is organized as follows. We first report a couple of verification analyses aimed to ensure that we could replicate the resting-state correlations between pupil size and whole-brain BOLD patterns reported in previous studies, and to assess the signal quality within the subcortical nuclei. Then, we attempt to reproduce the pupil-LC coupling that was reported in Murphy et al. (2014) by applying their convolution approach and LC localization method, as well as by interrogating the signal within our group LC ROI. After this, we move on to report three key analyses of pupil-AAS coupling aimed at understanding the temporal relationship between the two as well as the nature of this relationship: (i) an analysis in which we account for region- and participant-specific HRF differences in the convolution approach of the pupil time series; (ii) an analysis in which we explore pupil-AAS coupling while systematically adjusting the TTP of the HRF; and (iii) a cross-correlation analysis and cross spectral power density analysis in which we explore the possibility that, during rest, the temporal relationship between pupil size and AAS BOLD patterns is not mediated by the HRF typically used in event-related fMRI design.

Whole-brain pupil-BOLD patterns consistent with previous studies

We aimed to verify that our data showed the expected pupil-associated BOLD response patterns at the level of the cortex, cerebellum and subcortical parts of the limbic system. To this end, we followed as closely as

possible the approaches from two previous studies reporting pupil-BOLD coupling during rest (Murphy et al., 2014; Schneider et al., 2016) and indeed largely replicated their findings. First, following the approach by Schneider et al. (2016), we used pupil size (1-s shift) as a regressor in a GLM and convolved it with the canonical HRF (i.e., 6-s TTP). The assumption here is that the neural activity associated with spontaneous changes in pupil size is transformed into resting-state BOLD signal according to the same impulse response function as that driving neurovascular coupling during task performance. Indeed, we found positive correlations in the thalamus and negative correlations in the visual cortex and sensorimotor areas, as well as in the precuneus, cuneus, insula, superior temporal gyrus, and parahippocampal gyrus. These patterns of activation are consistent with those reported by Schneider et al. (2016; Figure 1a and Table 1). Second, we carried out the analysis in line with Murphy et al. (2014), using pupil size (not shifted) as a regressor and convolving it with the canonical HRF (i.e., 6-s TTP) as well as its temporal and dispersion derivatives (Figure 1b and Table 2). Adding these derivatives allows the timing of the HRF response peak and the width of the HRF response to vary across the whole brain. Here, we found significant clusters in the visual cortex, the insula, the anterior cingulate gyrus, and the inferior frontal gyrus, consistent with what was reported by Murphy et al. (2014). Overall, we found pupil-related BOLD response patterns across the whole brain that were highly consistent with the ones reported by the previous two studies.

Following Murphy et al's. (2014) approach, we also inspected pupil-associated activity in the LC. However, we did not find significant voxels when using our group LC mask as an ROI or when we applied the more liberal mask used by (2014; Keren et al., 2009; 2-SD version). Thus, contrary to Murphy et al. (2014), we were unable to replicate pupil-LC BOLD coupling using the same convolution methods.

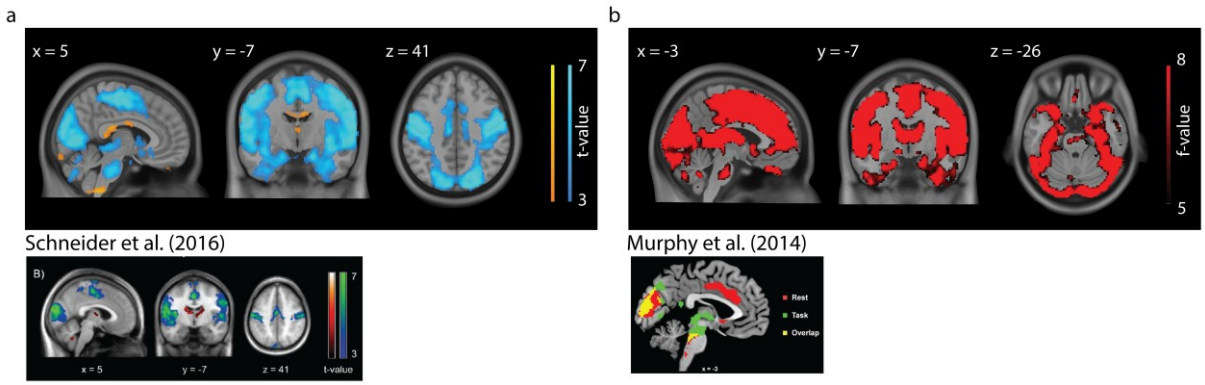

Figure 1. Whole-brain pupil-BOLD coupling in comparison to previous studies. *Neural correlates of pupil size from the analysis using the convolution approach from (a) Schneider et al. (2016)* and *(b) Murphy et al. (2014). Note that we only refer to the red and yellow activation in the figure from Murphy et al. (2014). Statistical parametric maps are thresholded at p < .001, uncorrected, for visualization purposes only. Whole-brain cluster-level FWE-corrected inferential statistics, in MNI space, are reported in Table 1 and 2.*

Table 1. Regions showing pupil-BOLD coupling using the convolution methods from Schneider et al. (2016)

	Cluster	
	K	p_{corr}
Positive		
Thalamus (R), Posterior cingulate cortex (R/L)	871	<.001
Rectus (L)	199	.010
Cerebellum (R)	142	.043
Cerebellum crus (L)	250	.003
Negative		
Cerebellum crus (R/L), cerebellum 6 (R/L), cerebellum 4/5 (R/L), (lingual gyrus (R/L), calcarine (R/L), fusiform gyrus (R/L), cuneus (R/L), precuneus (R/L), cerebellum 4 + 5 (L), cerebellar vermis, hippocampus (R/L), parahippocampal gyrus (R), amygdala (R/L), thalamus (R), superior occipital gyrus (R/L), middle occipital gyrus (R/L), inferior occipital gyrus (R/L), superior parietal gyrus (L), inferior temporal gyrus (R/L), middle temporal gyrus (R/L), superior temporal gyrus (R/L), insula (R), postcentral gyrus (L), precentral gyrus (L), paracentral lobule (R/L), supplimentary motor area (R/L), middle cingulate gyrus	65223	<.001

Note. Reported clusters survived whole-brain family-wise error (FWE) correction at the cluster level (p_{FWE} = .05). Abbreviations: R = right, L = left, p_{corr} = whole brain corrected cluster p-values, k = cluster size.

Table 2. Regions showing pupil-BOLD coupling using convolution methods from Murphy et al. (2014)

	Cluster	
	K	p_{corr}
Middle occipital gyrus (R/L), superior occipital gyrus (R/L), calcarine gyrus (R/L), cuneus (R/L), precuneus (R/L), angular gyrus (R/L), fusiform gyrus (R/L), cerebellum (R/L), middle temporal pole (R/L), inferior temporal pole (L), insula (R), inferior parietal lobule (R/L), superior parietal lobule (L), postcentral gyrus (R/L), middle frontal gyrus (R/L), medial frontal gyrus (R/L), inferior frontal gyrus (R/L), superior frontal gyrus (R/L), posterior cingulate gyrus, middle cingulate gyrus, anterior cingulate gyrus, supplementary motor area (R/L), middle frontal orbital (R/L), inferior frontal orbital (R/L), cerebellum crus II (R/L), cerebellum crus I (R/L), cerebellum 8 (R/L), cerebellum 9 (R/L), Pons	91471	<.001
Rectus (R/L)	146	.010

Note. Reported clusters survived whole-brain family-wise error (FWE) correction at the cluster level (p_{FWE} = .05). Abbreviations: R = right, L = left, p_{corr} = whole brain corrected cluster p-values, k = cluster size.

Assessment of the quality of subcortical fMRI data

To assess the quality of the subcortical functional data we extracted the tSNR from each ROI (see *Methods*). The average tSNR across the AAS ROIs (Figure 2b; range: 23.3 - 72.9) and cortical regions (range: 49.6 - 106.3) were in line with previous reports (Brooks et al., 2013, Figure 1: brainstem range: ~1-50 and cortex range ~50-112; Sing et al., 2022, supplementary Figure 6: brainstem range: 0-50, cortex range: 0-50). We also replicated a recently reported pattern of positive (partial) correlations among the signal fluctuations in each pair of

subcortical ROIs, controlled for activity in the pons (Figure 2c; van den Brink et al., 2019; see also Singh et al., 2022). Only the correlation between the DR and VTA was negative. Therefore, we are confident that the data had sufficient tSNR in our AAS ROIs to be able to assess pupil-AAS coupling.

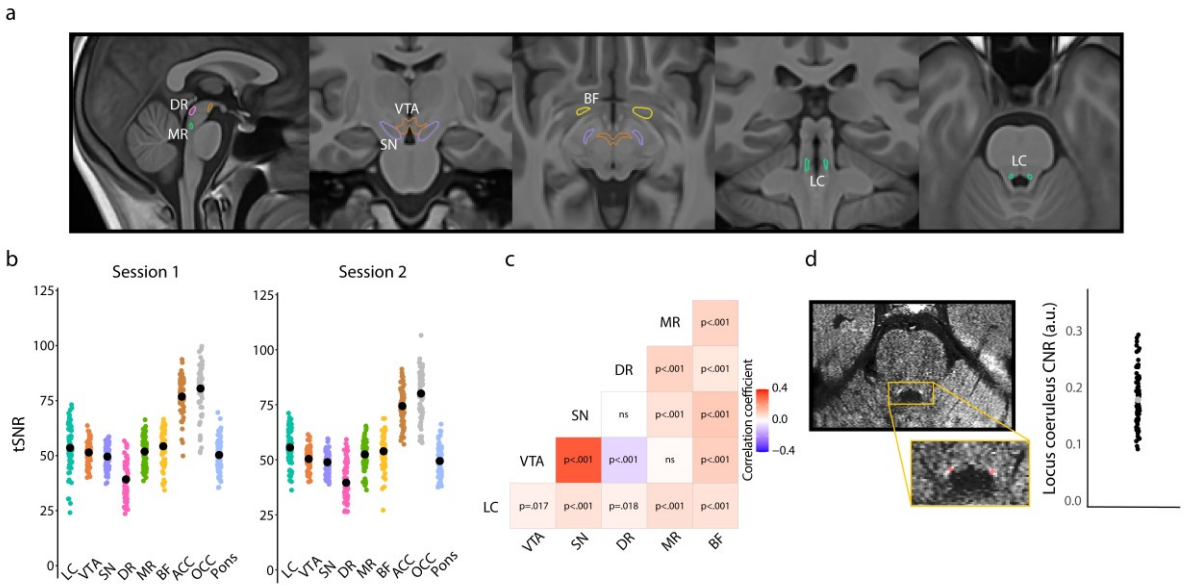

Figure 2. Overview of region-of-interest definition and validation of the quality of subcortical fMRI data. *(a) All subcortical ROIs overlaid on the group T1 template. (b) Individual data points showing the temporal signal-to-noise ratio for each ROI for session 1 (left) and session 2 (right; black points indicate the mean). (c) Correlation matrix showing that activity in subcortical nuclei co-varied positively with activity in other subcortical nuclei, with the strongest coupling present between the VTA and SN, which is to be expected given their close proximity, and the weakest (negative correlation) between the VTA and DR. Note: correlations were FDR-corrected and controlled for activity in the pons. (d) FSE image of an example participant. Hyperintensities corresponding to the LC are visible in the yellow box (top). Using the FSE images, the LC (red) was manually delineated on the individual level following established protocols (Clewett et al., 2016; Mather et al., 2017). The graph shows the LC contrast-to-noise ratio for all participants. The grey dot indicates the grand mean. Abbreviations: LC – locus coeruleus, VTA – ventral tegmental area, SN – substantia nigra, DR – dorsal raphe, MR – medial raphe, BF – basal forebrain ACC – anterior cingulate cortex, OCC – calcarine sulcus, CNR – contrast-to-noise ratio.*

No pupil-AAS coupling using region- and participant-specific estimates of the HRF

The methods that have previously been used to examine co-fluctuations between pupil size and fMRI BOLD patterns worked under the assumption that the shape of the HRF during rest is homogeneous across the whole brain (Breeden et al., 2016; DiNuzzo et al., 2019; Schneider et al., 2016; Yellin et al., 2015). This assumption

may not be correct, and because even a 1-s latency difference between assumed HRF and actual HRF can have a significant impact on fMRI results (Wall et al., 2009), it may be important to account for regional and individual differences (Handwerker et al., 2004) in the shape of the HRF. Indeed, subcortical structures have been characterized by faster BOLD responses (TTP 4 – 5 s; Lau et al., 2011; Lewis et al., 2018; Yen et al., 2011) compared to the cortex (TTP 5 – 6 s; Lewis et al., 2018; Friston et al., 2000). Therefore, we next estimated ROI-specific and participant-specific HRFs using an approach in which spontaneous pseudo-events were identified in our resting-state data and then aligned to determine the delay between the pseudo-events and corresponding BOLD signatures (Rangaprakash et al., 2018; Wu et al., 2013). The number of detected pseudo-events per ROI is shown in Figure 3c. Note that for some participants only one session was used to estimate these HRFs, so the number of detected pseudo-events for these participants tended to be smaller.

After carrying our pairwise comparisons, we found that, as expected, the TTP of the estimated HRFs was significantly faster for all subcortical AAS ROIs than for each of the two cortical ROIs ($M_{\text{subcortical ROIs}}$ = 4.7 s, $SD_{\text{subcortical ROIs}}$ = 0.6 s, $M_{\text{cortical ROIs}}$ = 5.4 s, $SD_{\text{cortical ROIs}}$ = 0.8 s; Figure 3d). The pupil-BOLD analysis using these specific HRFs, however, revealed no significant pupil-AAS correlations (Figure 3g, 3h). We only found that pupil size correlated negatively with activation in the OCC (p_{corr} < .001 [pupil size], p_{corr} = .018 [pupil derivative], FDR-corrected). Note that the negative sign of this correlation is consistent with what we reported above and with previous reports linking pupil size to decreased activity in the visual system (Schneider et al., 2016; Yellin et al., 2015).

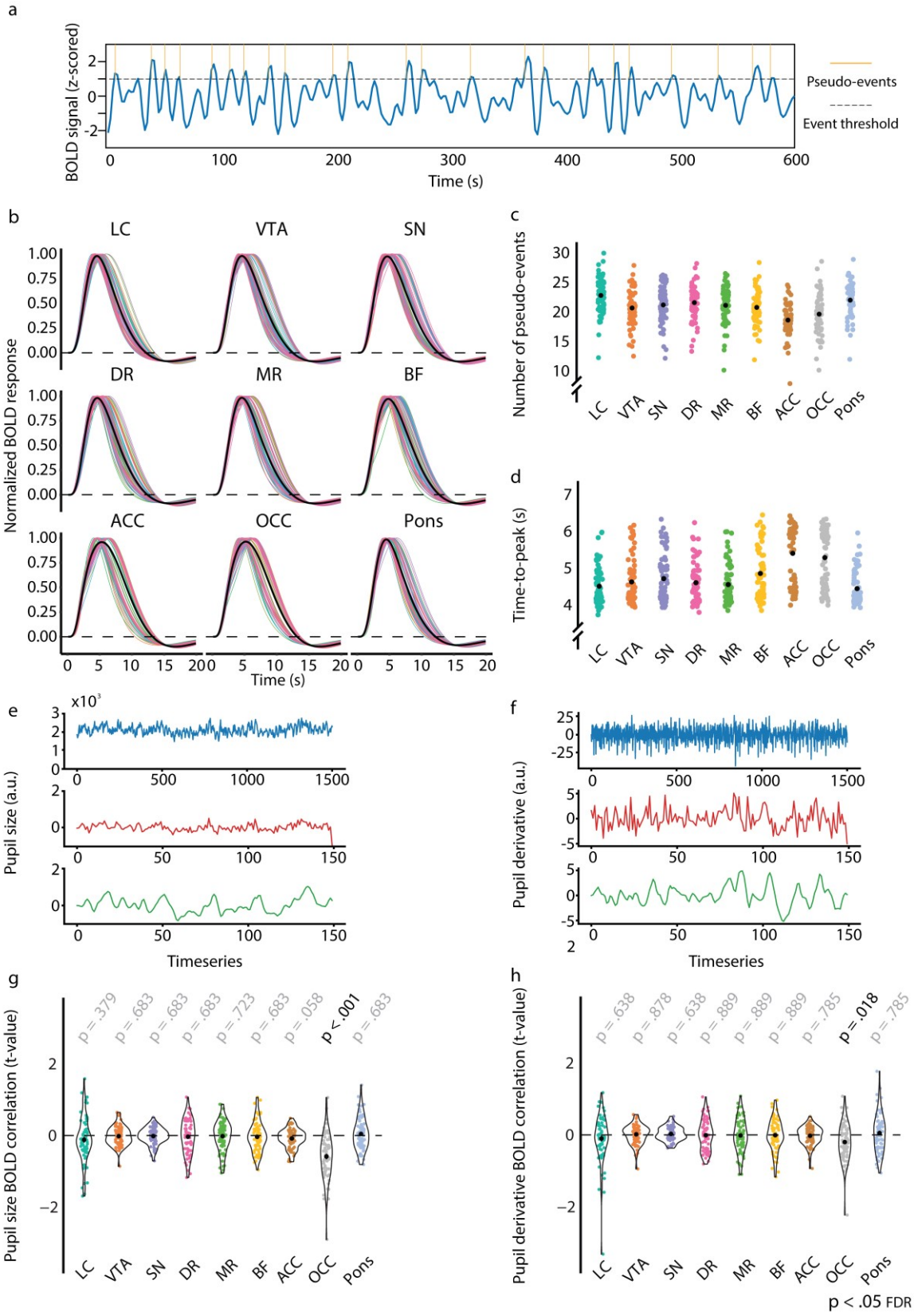

Figure 3. Overview of the analysis using region- and participant-specific estimates of the HRF. *(a) One participant's pre-processed LC BOLD signal (concatenated across the two sessions), evaluated against a chosen threshold (>1 SD) to extract onsets of spontaneous neural events (indicated in yellow). (b) Estimated hemodynamic response functions (HRFs) for each participant and ROI. Black lines indicate the average across*

participants. (c) The number of spontaneous neural events that were used to estimate the region- and participant-specific HRFs. Black dots indicate the mean. (d) Time-to-peak (TTP) of the HRF for each participant and ROI. Black dots indicate the average across participants. Overview of the pupil data processing pipeline of one randomly chosen participant for pupil size (e) and the pupil derivative (f). The plots portray the raw pupil data (blue), the pupil time series down-sampled to the TR (red), and the convolved pupil time series (for LC HRF, green). The extracted t-values from the first-level resting-state HRF analysis for pupil size (g) and the pupil derivative (h). P-values refer to one-sample t-tests (difference from zero; FDR-corrected). Abbreviations: LC – locus coeruleus, VTA – ventral tegmental area, SN – substantia nigra, DR – dorsal raphe, MR – median raphe, BF – basal forebrain, ACC – anterior cingulate cortex, OCC – calcarine sulcus.

In sum, the use of region- and participant-specific HRFs also did not result in significant pupil-AAS coupling. Importantly, by focusing on pseudo-events in the fMRI data, this approach still assumes that neurovascular coupling during rest (and other passive conditions) is characterized by the typical sluggish HRF used in event-related fMRI design.

Positive pupil-AAS coupling using HRFs with rapid time-to-peaks

Since the analysis strategy so far unexpectedly did not result in pupil-AAS coupling, we let go of the assumption of a relatively slow HRF similar to that driving neurovascular coupling during task performance. Therefore we further examined a potential relationship between pupil and AAS ROIs by examining how *systematically* varying the TTP (from 1 s to 6 s) of the default canonical HRF affected the coupling between pupil dynamics and our AAS ROIs. This analysis was inspired by a recent animal study (Pais-Roldán et al., 2020) showing that pupil-BOLD signal coupling dynamics vary across time.

We found that for almost all AAS ROIs the strength of pupil-BOLD coupling differed across TTPs (main effect of TTP; LC: $p < .001$, VTA: $p < .001$, SN: $p < .001$, MR: $p = .043$, BF: $p = .009$, FDR-corrected for nine ROIs). The overall pattern shows that coupling between pupil size and AAS BOLD patterns increases with earlier TTPs. Specifically, we found positive correlations for all AAS regions at earlier TTPs (especially the 1-s [Figure 4a] and 2-s TTPs) but no significant correlations (LC, VTA, SN, DR, MR) at later TTPs (5 s to 6 s; Figure 4b). For the OCC ROI, we found a positive correlation at the 1-s TTP, followed by a shift to negative correlations at later TTPs (4 s to 6 s), which is in line with previous work (Breeden et al., 2016; Schneider et al., 2016; Yellin et al., 2015) and the results we reported above (*Whole-brain pupil-BOLD patterns consistent with previous studies*), whereas the ACC correlated positively with pupil size at predominantly early TTPs (1 s to 4 s; Figure 4c; 4d), similar to the AAS ROIs.

Similar analyses for the pupil derivative also showed significant differences in the strength of pupil-BOLD coupling across the TTPs for the VTA ($p = .012$), SN ($p = .022$), DR ($p = .002$), ACC ($p = .009$), and OCC ($p < .001$; FDR-corrected for nine ROIs). The overall pattern and follow-up *t*-tests revealed similar, but attenuated effects

in comparison to pupil size (Figure S2a). The most prominent exception was the OCC, which showed a curvilinear relationship with largest correlations for intermediate TTPs (2s to 5s), which is also visible upon inspecting the whole-brain maps in Figure S2b. The same analyses carried out for the control region in the pons revealed no main effect of TTP for pupil size or the pupil derivative, nor were there any positive or negative associations with pupil size or the pupil derivative for any TTP, attesting to the specificity of the pupil-BOLD associations found in our AAS and cortical ROIs. Statistical parametric maps including whole brain results for all TTPs are shown in Figure 4d and Figure S2b.

These exploratory analyses suggest that fluctuations in pupil diameter have a much closer temporal relationship with changes in AAS-BOLD activity than what is characteristic of event-related responses.

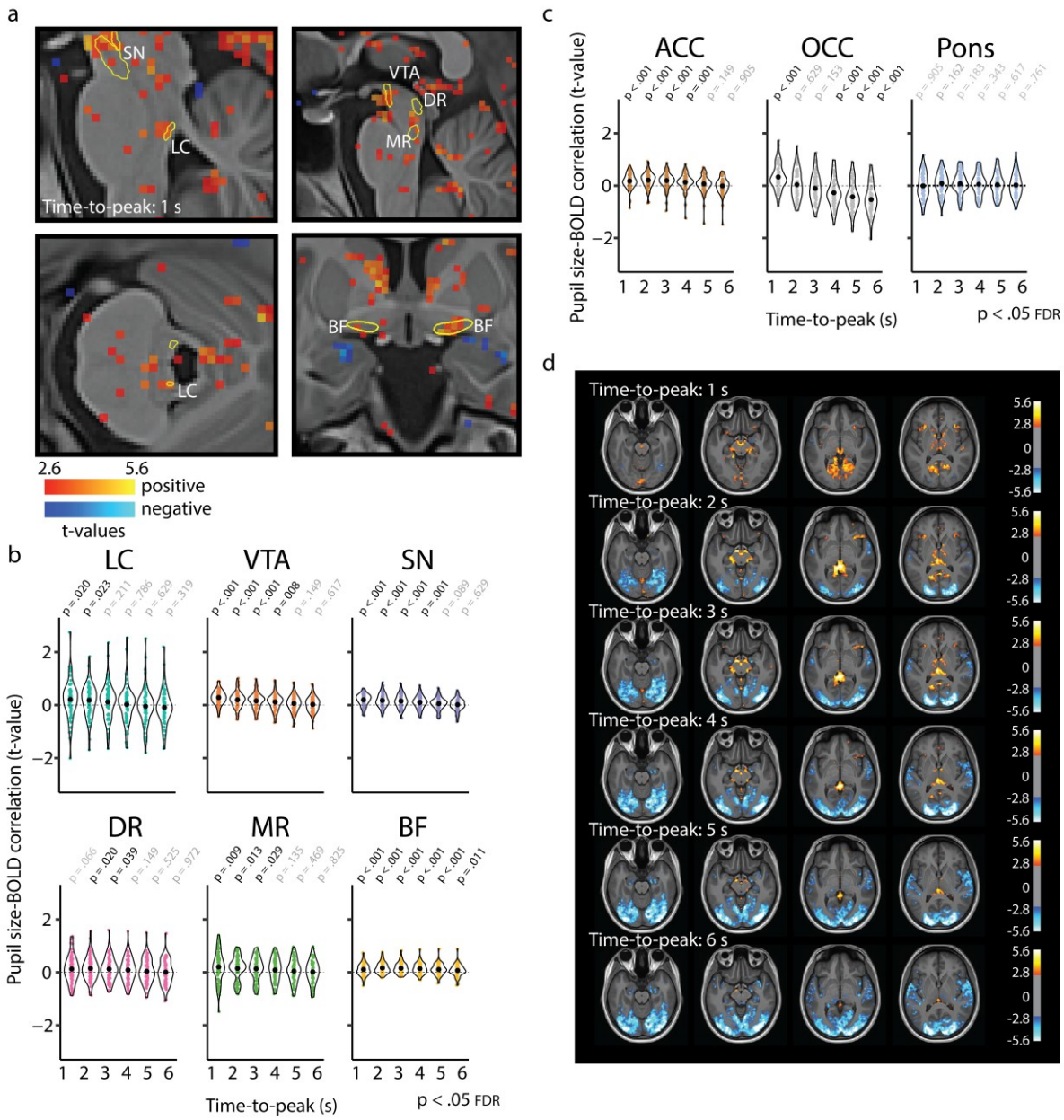

Figure 4. Pupil-BOLD correlations based on systematic adjustment of the time-to-peak of the HRF. *(a) Statistical maps showing pupil-BOLD correlations in the subcortex for the 1-s TTP. Graphs show the extracted t-statistics as a function of the systematically adjusted TTP for each participant in the subcortical ROIs (b) and the validation and control ROIs (c). P-values refer to one-sample t-tests (difference from zero; FDR-corrected). Black dots indicate the mean. (d) Statistical maps showing unsmoothed pupil-BOLD correlations across the cortex for each TTP (1 s to 6 s). All statistical maps were thresholded at p < .005 (uncorrected) for visualization purposes only. Abbreviations: LC – locus coeruleus, VTA – ventral tegmental area, SN – substantia nigra, DR – dorsal raphe, MR – median raphe, BF – basal forebrain, ACC – anterior cingulate cortex, OCC – calcarine sulcus.*

Positive pupil-AAS coupling when BOLD patterns closely follow pupil fluctuations

In our next analysis we wanted to release the assumption that BOLD responses associated with pupil-size changes would resemble an HRF. Therefore, we correlated the BOLD signal from our AAS ROIs with the *unconvolved* pupil vector using a cross-correlation approach (Pais-Roldán et al., 2020; Yellin et al., 2015). This method also allowed us to interrogate the pupil-BOLD coupling in both time directions. To that end, we shifted the pupil vector 8 s backwards and forwards, in steps of 2 s, with negative lags (backwards) corresponding to pupil changes preceding the BOLD signal, and positive lags (forwards) corresponding to pupil changes succeeding the BOLD signal (Figure 5).

Critically, and in line with the TTP analysis, we found significant positive pupil-BOLD correlations for all AAS ROIs (except the DR), with the strongest correlations occurring at lag 0 (Figure 5). These results again suggest that the relationship between pupil size and AAS activity is temporally close, rather than following the shape of an HRF with a 5- or 6-s TTP. In addition, these patterns of results appeared to be stable across the two sessions (Figure S3). For the pupil derivative (Figure S4), we observed a similar pattern in SN and VTA, with stronger correlations at lag 0, although overall the correlation coefficients were attenuated compared to those for pupil size, or not present in some AAS ROIs (LC, MR, and BF).

For comparison, we also computed cross-correlations between pupil size and BOLD signal extracted from our validation and control ROIs (ACC, OCC, pons; Figure 5). The OCC showed strong negative correlations at lags +4 to +8 s, similar to previous studies (Murphy et al 2014; Schneider et al 2016), and in line with the replication and TTP analyses reported above. However, the OCC also showed a positive correlation with pupil size at short lags (-2 s to +2 s). Similarly, we found that both ACC and OCC correlated most strongly with the pupil derivative (Figure S4) at relatively short positive lags (0 s to +4 s), with a shift to a strong negative correlation at maximum positive lags (+8 s), especially in the OCC.

Together, the TTP analysis and cross-correlation analysis yield essentially the same outcome, suggesting that no HRF convolution is needed to characterize the relationship between pupil size and AAS BOLD patterns during rest.

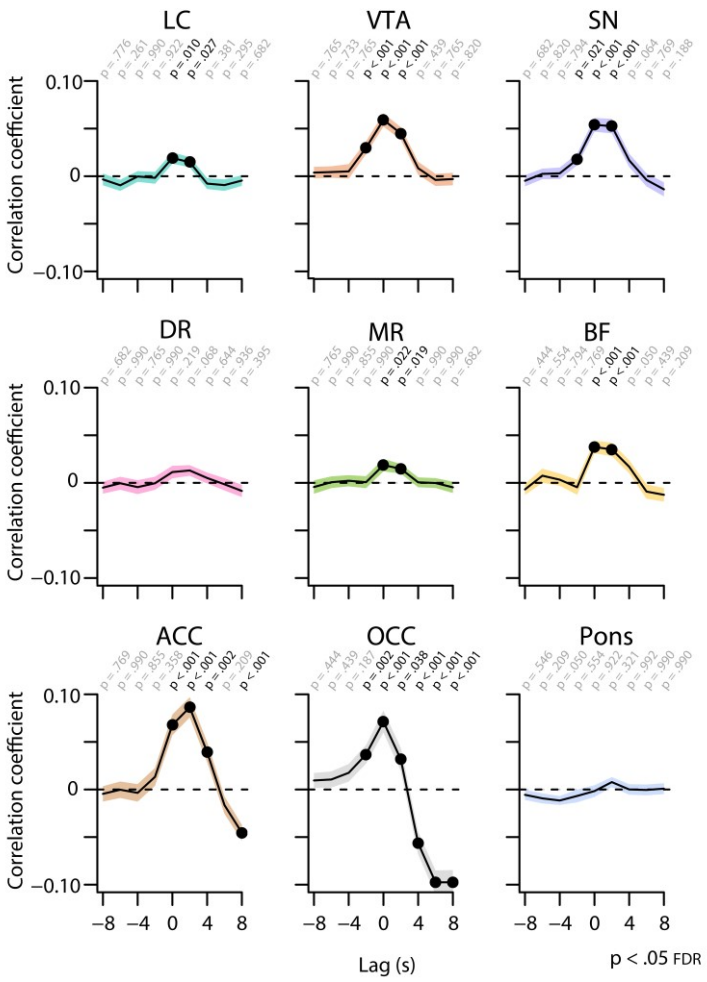

Figure 5. Cross-correlations between the unconvolved pupil time series and the BOLD time series at various time lags. *Negative (positive) time lags indicate that the pupil signal precedes (follows) the BOLD signal. Black lines indicate the grand mean and shaded regions indicate the standard error of the mean. P-values refer to one-sample t-tests for the corresponding time bin. Black font and black dots indicate significant time bins (p < .05, FDR-corrected).*

Pupil-AAS coupling is largely driven by oscillations in low-frequency band

Finally, to better understand the nature of the pupil-AAS coupling, we carried out an exploratory cross-spectral density analysis (Figure 6). The cross power spectral density is the Fourier transform of the cross-correlation functions reported above, and hence expresses the relationship between the pupil and AAS signals in the frequency domain. To determine which frequency bands were driving the observed positive pupil-AAS correlations, we calculated the cross spectral power density (see *Methods*) of the pupil size time series and average BOLD time series extracted from each ROI. A simple peak detection indicated that the correlations for most AAS nuclei and both cortical ROIs (ACC and OCC) were largely driven by frequencies between 0.04 and 0.09 Hz (LC: 0.09, VTA: 0.04, SN: 0.03, DR: 0.008, MR: 0.04, BF: 0.04, ACC: 0.04, OCC: 0.07; Figure 6a; 6b).

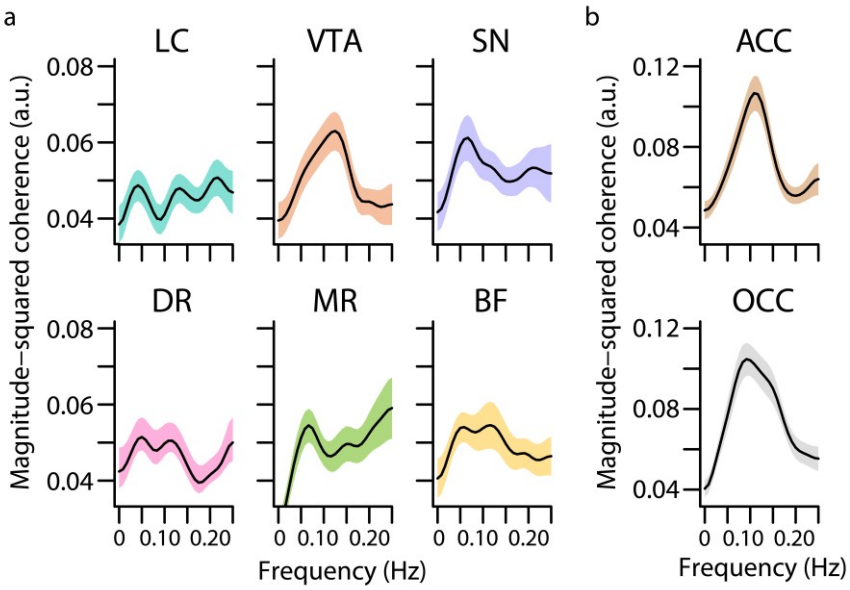

Figure 6. Cross spectral power density analysis. *Cross spectral power density for subcortical ROIs (a) and cortical ROIs (b) averaged across participants. Black lines indicate the grand mean and shaded regions indicate the standard error of the mean. Abbreviations: LC – locus coeruleus, VTA – ventral tegmental area, SN – substantia nigra, DR – dorsal raphe, MR – median raphe, BF – basal forebrain, ACC – anterior cingulate cortex, OCC – calcarine sulcus.*

Discussion

In the current study we examined whether, during rest, non-luminance-related spontaneous fluctuations in pupil size were associated with fluctuations in BOLD signal in nuclei part of the ascending arousal system (AAS). We found a positive correlation between pupil size and BOLD signal in all of the AAS ROIs: LC, VTA, SN, DR, MR and (sublenticular) BF. This finding is in line with recent rodent studies (Joshi et al., 2016; Reimer et al., 2016) indicating that pupil changes reflect activity in multiple neuromodulatory systems, not only the noradrenergic system. Critically, using two different methodological approaches, we found that pupil-AAS coupling was strongest when the two signals were assumed to occur close in time. This means that during rest, unlike in response to task events (de Gee et al., 2017), BOLD signal fluctuations in AAS nuclei immediately follow fluctuations in pupil size. This correlation was largely driven by slow oscillations (i.e., ~0.05 – 0.1 Hz) in both measures. Together, our results suggest that pupil size can be used as a noninvasive readout of AAS activity, and reveal new insights into the temporal dynamics of pupil-AAS coupling during rest.

We found robust positive correlations between pupil size and BOLD signal in five of our AAS ROIs: LC, VTA, SN, MR and (sublenticular) BF. The positive relationship with pupil size was less robust for the DR, and only

significant in the TTP analyses, perhaps because this area had lower tSNR than the other subcortical ROIs. Thus, unlike what findings from previous studies (e.g., Murphy et al., 2014) may have implicitly suggested, the coupling between pupil size and activation of the AAS is not specific for the LC. Our findings contribute to a growing body of literature showing a more general role for AAS nuclei in driving pupil size changes. Specifically, our findings are consistent with recent animal studies that found co-fluctuations in pupil size and LC and BF activity during rest (Joshi et al., 2016; Reimer et al., 2016); with studies showing that optogenetic activation of the LC or DR increases pupil size (Breton-provencher & Sur, 2019; Cazettes et al., 2021); and with human task-related fMRI work showing positive correlations between event-related pupil responses and BOLD responses in the LC, VTA and BF (de Gee et al., 2017). Unfortunately, it has become common practice for researchers to interpret task-related pupillometry data in terms of the role of the LC in cognitive and brain function. However, our findings reinforce previous arguments (Joshi & Gold, 2020) that changes in pupil size should not be used to infer a selective role for the LC. An outstanding question is to what extent the AAS nuclei have *independent* influences on pupil size.

The temporal relationship between pupil size and AAS BOLD response patterns was different than we had expected based on reports from previous resting-state and event-related fMRI studies (e.g., de Gee et al., 2017; Murphy et al., 2014). Namely, we found that BOLD signal in the AAS closely followed the corresponding pupil fluctuations. These results were corroborated by a series of analyses in which we convolved the pupil time series with HRFs with systematically varied TTP (1-6 s). Pupil time series that were convolved with the canonical HRF (TTP = 6 s) or region-specific HRFs based on a point process approach were not significantly related to AAS activation. Instead, maximal and significant pupil-AAS coupling was found using HRFs with TTPs of 1 to 3 seconds. In addition, cross-correlations between the unconvolved pupil time series and AAS BOLD time series similarly revealed maximum correlations when the signals occurred close in time (at lags of 0 to 2 seconds). For the pupil derivative we obtained similar results, with strongest cross-correlations around lag 0 s to +2 s, although the correlation coefficients were overall attenuated and only remained significant in the VTA and SN. Our findings are in line with previous research that has suggested that subcortical regions (Lewis et al., 2018) and AAS nuclei (de Gee et al., 2017) are characterized by faster event-related hemodynamic responses than cortical regions. However, our findings suggest an even closer temporal relationship between pupil size and BOLD response patterns in AAS nuclei during rest. Therefore, these findings, although correlational, have implications for our understanding of the time scale at which AAS regions might drive changes in pupil diameter.

Furthermore, our findings may provide a reason why most previous human resting-state pupil-fMRI studies (e.g. Breeden et al., 2016; Schneider et al., 2016; Yellin et al., 2015) did not find or report pupil-AAS coupling. Namely, these studies only investigated pupil-BOLD coupling with longer time lags between pupil changes and corresponding BOLD response patterns. Using standard TTPs we (broadly) replicated previously reported associations between pupil size and cortical BOLD response patterns (e.g., negative coupling with the visual cortex, positive coupling with the thalamus and posterior cingulate cortex; e.g., Murphy et al., 2014; Schneider et al., 2016; Yellin et al., 2015). However, we did not find evidence that standard TTPs characterized

the coupling between resting-state pupil size and AAS activation. Although one of these previous studies did report pupil-LC coupling (Murphy et al., 2014), we were unable to replicate this finding in our data, despite using the same convolution methods, LC mask, and other methodological details of this study, and despite a much larger sample size (70 versus 14 included participants). Although we cannot make a direct comparison between the shape of human and mouse HRFs, a recent study in rats (Pais-Roldán et al., 2020) also found temporally close positive coupling (i.e., 1-s TTP) between resting-state pupil dynamics and BOLD signal in specific areas in the brainstem including the A5 noradrenergic cell group (which projects to the spinal cord). They, however, did not find evidence for a coupling between pupil dynamics and any of the AAS nuclei. Although this seems inconsistent with our findings, note that the rats in this study were anesthetized. Indeed, preliminary evidence suggests that behavioral states can strongly modulate pupil-AAS coupling (Megemont et al., 2022), and therefore it is possible that in an anesthetized state pupil-AAS coupling is reduced or absent.

Lastly, our findings raise the question *how* the neuronal activity in AAS nuclei that contributes to resting-state pupil fluctuations is coupled to the BOLD signal in these areas. The main frequency band that drove our pupil-AAS coupling was ~0.05-0.1 Hz. Interestingly, recent work in the mouse cortex has shown that the ultra-slow (~0.1 Hz) BOLD fluctuations that are characteristic of resting-state fMRI data are entrained by ultra-slow vasomotor oscillations that lead to rhythmic changes in the diameter of brain arterioles. These vasomotor oscillations, in turn, are entrained by rhythmic local neuronal activity in the same ultra-low-frequency band (Drew et al., 2020; Mateo et al., 2017). These findings beg the question whether this neurovascular coupling sequence may be responsible for our findings. However, in the mouse brain this sequence, from neuronal activity and vasomotion to blood oxygenation levels, was estimated to last approximately 2.6 s (Mateo et al., 2017). This seems inconsistent with the 0- to 2-s interval between our estimated timing of the AAS neuronal activity underlying pupil fluctuations and the timing of corresponding AAS BOLD signals. Future work in animal models should therefore examine the physiological basis of these seemingly close temporal relationships between activity of AAS nuclei and corresponding changes in pupil size by simultaneously measuring pupil size changes and rhythmic BOLD fluctuations during awake rest.

Our study has several potential limitations. First, although our EPI sequence had a higher spatial resolution (2 mm isotropic) than previous studies linking pupil size to BOLD (e.g., 3.5 mm isotropic in Murphy et al., 2014), imaging small subcortical structures at this conventional spatial resolution may have led to partial-volume averaging (Forstmann et al., 2017; Liu et al., 2017a), especially in the LC, the smallest of our ROIs. To mitigate this concern, we did not apply spatial smoothing to the EPI data. Our confidence in the LC imaging data reported here is also bolstered by the fact that the LC showed the same pattern of results as other, much larger nuclei, including the VTA, SN and BF, that are less susceptible to partial-volume averaging effects. We also note that a further increase in spatial resolution at 3T would be accompanied by a dramatic drop in signal-to-noise ratio (Murphy et al., 2007), and therefore would not per se lead to a better signal from the AAS regions. Although future studies combining pupillometry with ultra-high-field fMRI (e.g., 7T) could circumvent this problem, measuring pupil size in ultra-high-field scanners is still challenging. A second potential limitation concerns the

proximity of some of the subcortical ROIs to air- and cerebrospinal fluid-filled cavities as well as major arteries, making them particularly prone to movement and other sources of physiological noise (Brooks et al., 2013). To mitigate this concern, we included an extensive physiological noise correction model, accounting for measured cardiac and respiratory signal components as well as residual signal from the fourth ventricle. Furthermore, if the BOLD signal in AAS nuclei was largely driven by noise, this could not explain the robust temporal relationship between AAS BOLD and pupil size, and the selective absence of pupil-BOLD coupling in the pons, our control region that is also susceptible to physiological noise artifacts. A third drawback is that our analyses were limited by the temporal resolution of our fMRI data. Due to our 2-s TR we were unable to interrogate potentially meaningful, faster pupil-BOLD correlations. Future studies using ultra-high-field fMRI and/or simultaneous imaging techniques (Barth et al., 2016; Lewis et al., 2016) can speed up image acquisition and assess the presence of pupil-BOLD correlations at a faster timescale.

In conclusion, we show that spontaneous changes in pupil size that occur during rest reflect activity in a variety of nuclei that are part of the AAS. This suggests that pupil size can be used as a noninvasive and general index of AAS activity, in contrast to previous work suggesting a selective role for the LC in arousal-related pupil size changes. However, the nature of pupil-AAS coupling during rest appears to be vastly different from task-related pupil-AAS coupling, which has previously been modeled using a canonical HRF. Together, our findings provide new insights into the nature and temporal dynamics of AAS-linked pupil size fluctuations.

Materials & Methods

This study was preregistered on the Open Science Framework before data analysis: osf.io/xcj2y. Note that preregistration occurred after data collection; due to circumstances surrounding the global pandemic, already collected data was used to address our hypotheses. As we could not replicate previous findings, we needed to deviate from the preregistration. When we deviated from the preregistration, this will be explicitly mentioned below.

Participants

Seventy-four right-handed participants were recruited from New York University (39 females, mean age: 22.5 years, age range: 18-33 years) and completed two resting-state sessions on two consecutive days. Exclusion criteria for participation were as follows: current treatment or treatment in the last year of psychiatric, neurological, or endocrine disease, current treatment with any medication, average use of >3 alcoholic beverages daily, average use of recreational drugs, habitual smoking, uncorrected vision, and contraindications for MRI. Two participants were excluded entirely and one session for one participant was excluded due to technical issues with the scanner. The two resting-state sessions were part of a larger study of which the data will not be reported here. The study was approved by the University Committee on Activities Involving Human Subjects at New York University (Institutional Review Board #2016-2) and the study was conducted in accordance with these guidelines

and regulations. All participants provided written informed consent. Participants received a payment ($35 per hour) for their participation.

Procedure

All participants completed two resting-state sessions of five minutes each, 24 hours apart (+/- 2 hours). During the session they were instructed to think of nothing in particular, let their mind wander but not to have any repetitive thoughts such as counting. They were instructed to keep their eyes open and maintain their gaze on a centrally presented fixation dot (RGB: 60, 60, 255) on a grey screen (RGB: 125,125,125).

MRI data acquisition

MRI data was acquired using a Siemens MAGNETOM Prisma 3T MR scanner. T2*-weighted BOLD images were recorded using a customized multi-echo EPI sequence with ascending slice acquisition (58 axial slices; TR = 2 s; TE = 14.4, 39.1 ms; partial fourier = 6/8; GRAPPA acceleration factor = 2; multiband acceleration factor = 2; flip angle = 65°; slice matrix size 104 x 104 mm; slice thickness = 2.0 mm; FOV: 208 x 208 mm; slice gap = 0; bandwidth: 2090 Hz/px; echo spacing: 0.56 ms). Multi-echo EPI protocols can be used to avoid the tradeoff between BOLD sensitivity in the cortex and subcortex (Turker et al., 2021). To account for regional variation in susceptibility-induced signal dropout, voxel-wise weighted sums of both echoes were calculated based on local contrast-to-noise ratio (Poser et al., 2006). A structural image (0.9 mm isotropic) was acquired using a T1-weighted 3D MP-RAGE (TR = 2.3 s; TE = 2.32 ms; flip angle = 8°, FOV = 256 x 256 x 230 mm). A fast-spin echo (FSE) neuromelanin-sensitive structural scan was acquired for delineation of the LC (11 axial slices , TR = 750 ms, TE = 10 ms, flip-angle = 120°, bandwidth = 220 Hz/Px, slice thickness = 2.5 mm, slice gap = 3.5 mm; in-plane resolution = 0.429 x 0.429 mm). Note that a large slice gap is a common feature in the use of FSE scans for LC imaging (Liu et al., 2017a). This procedure allows for a high in-plane resolution but with a thicker slice thickness, resulting in elongated voxels that match the cylindrical shape of the LC. To minimize excessive movement during scanning, we secured participants' heads in a pillow and medical tape was attached across their foreheads to provide immediate tactile feedback in case of any movement, which has been shown to reduce motion (Krause et al., 2019).

MRI data preprocessing

Preprocessing of MRI data was carried out using Advanced Normalization Tools v2.1 (ANTs) and SPM12 (https://www.fil.ion.ucl.ac.uk/spm; Wellcome Department of Imaging Neuroscience, London, UK). Here we deviated from the preregistration, as we reported we would carry out all preprocessing steps in SPM12. Since ANTs SyN was found to be the best performing method for normalization (Ewert et al., 2019), some steps, including standardization and registration, were carried out using ANTs instead,

476 A whole-brain group template *($T1_{template}$)* was generated using all MP-RAGE scans (using
477 antsMultivariateTemplateConstructinon2.sh; Figure S1a). This process involved two steps: 1) participants' whole-
478 brain T1 scans (*$T1_{native\ space}$)* were coregistered to a common group space (*$T1_{group\ space}$*); then 2) these coregistered
479 scans were averaged to form a whole-brain group template *($T1_{template}$)*. An initial fixed image was created by
480 averaging all input files. For registration (or 'normalization') of input images, a set of linear (rigid, then affine)
481 and nonlinear (SyN) algorithms were used. Each nonlinear registration was performed over four levels of
482 increasingly fine-grained resolutions (100x70x50x10 iterations). We applied a N4 bias field correction on moving
483 images before each registration (using *N4BiasFieldCorrection* function). Cross-correlation was the similarity
484 metric used for registration. Greedy SyN (SyN) was the transformation model used for registration. The gradient
485 step size for refining template updates was set at 0.20 mm. After the whole-brain template image *($T1_{template}$)* was
486 generated, for optimal coregistration, all individual MP-RAGE scans (*$T1_{native\ space}$*) were submitted to a new
487 coregistration step (using antsRegistration.sh; Figure S1b). For this we performed linear (rigid, then affine),
488 followed by nonlinear (SyN), registration steps, resulting in optimized individual whole-brain scans in template
489 space (*$T1_{group\ space}$*).

490 Mutual information maximization-based rigid-body registration was used to register MP-RAGE scans
491 and functional images. Functional images were motion-corrected using rigid-body transformations. To move the
492 functional images into group space, the affine transforms and displacement field transformations from the final
493 coregistration *($T1_{native\ space}$* to *$T1_{group\ space}$)* for each participant were applied to their respective functional images
494 (using linear interpolation). To avoid contamination of AAS BOLD activity by signal from adjacent structures, all
495 analyses reported in this paper, except those aimed at replicating previous studies (see section '*Comparisons*
496 *with previous studies*'), were performed without spatial smoothing.

497 We applied a movement and physiological noise correction model with 33 regressors in SPM12. These
498 included six movement parameter regressors (3 translations, 3 rotations) derived from rigid-body motion
499 correction, high-pass filtering (1/128Hz cut-off) and AR(1) serial autocorrelation corrections. In addition these
500 included retrospective image-based correction (RETROICOR) of physiological noise artifacts (Glover et al., 2000)
501 regressors. Raw pulse was preprocessed using PulseCor (https://github.com/lindvoo/PulseCor) implemented in
502 Python for artifact correction and peak detection. Fifth-order Fourier models of the cardiac and respiratory
503 phase-related modulation of the BOLD signal were specified (Van Buuren et al., 2009), yielding 10 nuisance
504 regressors for cardiac noise and 10 for respiratory noise. Additional regressors were calculated for heart rate
505 frequency, heart rate variability, (raw) abdominal circumference, respiratory frequency, respiratory amplitude,
506 and respiration volume per unit time (Birn et al., 2006), yielding a total of 26 RETROICOR regressors
507 (https://github.com/can-lab/RETROICORplus). An additional regressor was added to remove signal fluctuations
508 from the fourth ventricle, which was manually delineated using individual MP-RAGE scans (M= 90, SD=34 voxels).
509 This movement and physiological noise correction model was added to all general linear models (GLMs)
510 described below. Please note that we deviated from the preregistration and did not apply 'scrubbing' in addition
511 to the 33 nuisance regressors.

512

513 ***Pupil data acquisition and preprocessing***

514 Pupil size was recorded using an MR-compatible eye-tracker (EyeLink 1000 Plus; SR Research, Osgoode,
515 ON, Canada) at a sampling rate of 250 Hz. The eye-tracker was placed at the end of the scanner bore, such that
516 the participant's right eye could be tracked via the head coil mirror. Before the start of each resting-state session,
517 we began with a calibration of the eye-tracker using the standard five-point EyeLink calibration procedure.

518 Moments when the eye-tracker received no pupil signal (i.e., during eye blinks) were marked
519 automatically during acquisition by the manufacturer's blink detection algorithm. Pupil data was preprocessed
520 using PupCor (https://github.com/lindvoo/PupCor) implemented in Python. Missing and invalid data due to
521 blinks were replaced using linear interpolation for the period from 100 ms before blink onset to 400 ms after
522 blink offset. Following the automated interpolation procedure, the data were manually checked and corrected if
523 any artifacts had not been successfully removed. Two sessions from two separate participants were excluded
524 due to technical problems with the eye-tracker. To ensure the pupil data was of good quality, a session was
525 excluded from all analyses if the raw pupil data contained >25% invalid samples (marked automatically during
526 data acquisition by EyeLink's blink detection algorithm; *n* sessions *excluded* = 15). For the remaining sessions (*n*
527 sessions *included* = 126; *n* participants = 70, average proportion invalid samples = 6.4%) we computed pupil size
528 as well as the first-order derivative of the pupil size time series. The latter describes the slope of changes in pupil
529 size, where positive values reflect pupil dilation and negative values reflect pupil constriction. Because pupil size
530 lags behind the underlying neural activity in AAS nuclei (including the LC and DR; Cazettes et al., 2021; Joshi et
531 al., 2016; Liu et al., 2017b; Reimer et al., 2016), and in line with previous neuroimaging studies (Pfeffer et al.,
532 2022; Schneider et al., 2016; Yellin et al., 2015), we shifted the pupil time series one second back in time. This
533 step was only omitted when we attempted to replicate Murphy et al. (2014). Both pupil time series (i.e., pupil
534 size and pupil derivative) were then resampled to the TR (2 s) resolution (0.5 Hz). To detect further artefactual
535 samples, within each 2-s time bin, any sample +/-3 SD outside the time bin mean was removed, after which the
536 average of the corresponding time bin was recalculated from the remaining non-artefactual samples (percentage
537 samples recalculated = 0.04%; as in Murphy et al., 2014). The results of these pre-processing steps were two
538 pupil time series (pupil size and pupil derivative) that were equal in length to the number of fMRI volumes (i.e.,
539 150) collected in each session.

540

541 ***Definition of regions-of-interest (ROIs)***

542 The LC was delineated on each participant's FSE scan using ITK-SNAP (version 3.8.0; Yushkevich et al.,
543 2006). Two raters (BL and a research assistant) manually identified LC voxels following established protocols
544 (Clewett et al., 2016; Mather et al., 2017). Pairwise dice similarity coefficients between both raters were high (M:
545 0.96, range: 0.70 – 1.00). As described in Clewett et al. (2016), left and right LC regions were identified in the
546 axial slice ~7 mm below the inferior colliculus. Within this slice, two regions were delineated in the form of a
547 cross ~1.29 mm wide and ~1.29 mm high (3 x 3 voxels, see Figure 2d), covering the 1 – 2 mm of LC neurons in
548 this slice. The center voxel for each cross was placed on the voxel with the highest signal intensity that fell within

549 an area anatomically consistent with the location of the LC. If the peak voxel was located immediately adjacent
550 to the fourth ventricle, the center of the ROI was placed one voxel further away from the ventricle. This ensured
551 that the peak voxel but no fourth ventricle voxels were included in the ROI. To ensure we captured LC intensity
552 signal, we calculated an objective measure for comparisons namely contrast-to-noise ratios between the average
553 signal intensity in the LC relative to a pontine reference region. Contras-to-noise ratios were positive for all
554 participants, indicating that LC intensity was consistently higher than pontine intensity (M: 0.17, range: 0.08 –
555 0.29; Figure 2d). The obtained contrast-to-noise ratios were in line with previous reports (Clewett et al., 2016;
556 Mather et al., 2017). For three participants we could not delineate LC ROIs because movement led to poor-quality
557 FSE images. For these participants we used the group LC ROI (i.e., average of all individual LC ROIs in group space
558 thresholded at 2 SD above the mean). This group LC ROI was also used for visualization purposes. In line with
559 current standards (Yi et al., 2021), the LC masks were then transformed (using nearest neighbor interpolation)
560 into template space by applying the linear and nonlinear transformations from the final coregistration *($T1_{native}$*
561 *$_{space}$* to *$T1_{group\ space}$),* and resliced resulting in the final individual LC masks in functional space (range of size in
562 functional space: 1 – 7 voxels, M=3.4 , SD=1.3 voxels).

563 Published probabilistic atlases were used for the remaining subcortical ROIs as there are no established
564 protocols for individual segmentation of these regions: VTA (Trutti et al., 2021), SN (Alkemade et al., 2020), DR
565 (Beliveau et al., 2015), MR (Beliveau et al., 2015) and the sublenticular (Ch4) part of the BF (Eickhoff et al., 2005;
566 Zaborszky et al., 2008), which includes the cholinergic nucleus basalis of Meynert (see Figure 2a). All atlases were
567 originally in MNI space. To move the atlases into our study-specific template space, antsRegistration.sh (using
568 the same parameters as described above) was applied to generate the transformation matrices between MNI
569 space and template space, which were applied to each ROI mask. Each subcortical mask was then thresholded
570 and resliced to the functional space. In the preregistration, we reported that we would only be examining pupil-
571 BOLD coupling in the LC, VTA, and SN. We also opted to include the raphe nuclei and BF since recent evidence
572 shows that they are involved in driving pupil size during task behaviours (Cazettes et al., 2021; de Gee et al.,
573 2017).

574 Previous studies (Schneider et al., 2016; Yellin et al., 2015) have found a robust relationship between
575 pupil size and BOLD patterns in the occipital cortex (OCC) and anterior cingulate cortex (ACC). Therefore, we
576 included these two cortical regions as additional validation ROIs. Specifically, we obtained masks of the calcarine
577 sulcus in the OCC and ACC using the automated anatomical labeling atlas in SPM (Tzourio-Mazoyer et al., 2002).
578 Lastly, to explore the specificity of our pupil-AAS BOLD results, we delineated a cubic ROI in the medial part of
579 the basis pontis (pons), which served as a control region in which we did not expect to find pupil-BOLD coupling.
580 The same procedure as described above was carried out to move these masks from MNI space into our study-
581 specific template space.

582

583 ***fMRI data quality assessment***

584 *Comparisons with previous studies*

We wanted to ensure that we could replicate the resting-state correlations between pupil size and BOLD patterns reported in previous studies. First, we followed the methods of Schneider et al. (2016). We convolved the pupil size time series with the canonical HRF (6-s TTP [time-to-peak]). This single pupil regressor, along with the movement and physiological noise correction model were entered into first-level GLMs. Note that we only refer to the light condition in Schneider et al. (2016), since we did not assess other light conditions. Second, we followed the methods of Murphy et al. (2014). Here, we used the preprocessed pupil size time series and convolved that with the default canonical HRF, as well as its temporal and dispersion derivatives (Friston et al., 2000). The resulting three pupil time series were entered into a first-level GLM together with the movement and physiological noise correction model. For the Murphy et al. (2014) comparison analysis, the first-level single-subject contrast maps were submitted to a second-level random effects analysis (one-way ANOVA, three levels of pupil/basis functions). To interrogate pupil correlations within the LC, statistics were also carried at the second-level using small volume correction with our group LC mask and the LC mask (Keren et al., 2009) used by Murphy et al. (2014) as an ROI in SPM12. In line with the reports of Schneider et al. (2016) and Murphy et al. (2014), the analyses described here included spatial smoothing with a 6-mm full width at half maximum (FWHM) Gaussian kernel.

Assessment of the quality of subcortical fMRI data

Next, we assessed the signal quality within the subcortical nuclei to ensure we would be able to capture pupil-AAS coupling. First, we inspected the temporal signal-to-noise ratio (tSNR) of our data in all cortical and subcortical ROIs. To do this, the tSNR was calculated as the ratio of the mean and the standard deviation of the signal across the unsmoothed BOLD time series from the two sessions. We then averaged the resulting tSNR within each ROI. Second, we investigated if we could replicate previous work reporting co-fluctuations between activity in various subcortical ROIs during rest (van den Brink et al., 2019). The extracted BOLD signal from each ROI (LC, VTA, SN, DR, MR, BF, and pons as a control region) per session, per participant, was denoised (using the movement and physiological noise correction model described above) and demeaned and then entered into a partial correlation analysis. We computed a partial correlation for each pair of AAS nuclei, controlling for activity in the pons. Correlation coefficients underwent a Fisher *r*-to-*Z* transform and were then submitted to one-sample *t*-tests.

Pupil-AAS coupling analyses

To systematically examine pupil-AAS coupling, and to understand the temporal relationship between the two signals, we conducted a set of three main analyses. The rationale for our approach was that previous studies (see *Comparisons with previous studies*) assumed that pupil-brain coupling during rest would follow the canonical HRF used in event-related fMRI designs. However, these assumptions may not be correct or may not apply to subcortical nuclei. Therefore, in our first analysis we (i) convolved the pupil time series with participant-

specific and ROI-specific estimates of the HRF (described below in *Estimation of region- and participant-specific HRF*), which showed a range of TTPs. In the second analysis we (ii) systematically changed the TTP of the canonical HRF (from 1 to 6 s, in steps of 1 s) and convolved the pupil time series with each of these. And lastly, we (iii) performed a pupil-AAS cross-correlation analysis in which we did not convolve the pupil time series at all. Note that analyses (ii) and (iii) were not preregistered, as they were carried out to better understand the outcome of analysis (i). Therefore, they should be deemed exploratory. We will now provide a detailed description of each of these analyses.

Estimation of region- and participant-specific HRF

In the first main analysis, we aimed to account for HRF variability across different brain regions and participants in our resting-state data. Here, we deviated from the preregistration, in which we stated that we would obtain participant-specific HRFs from event-related fMRI data. However, the HRFs based on these event-related fMRI data did not provide plausible HRFs in the AAS regions (i.e., did not rise up to one tall peak and follow with an undershoot), possibly because these AAS regions may not have been involved in the task at hand. Instead, we used a blind deconvolution technique developed by Wu et al. (2013) to estimate region- and participant-specific HRFs based on the data from both resting-state sessions. This point process method has been validated on simulated as well as empirical data (Rangaprakash et al., 2018; Wu et al., 2021). It assumes that a common HRF is shared across various spontaneous point process events (i.e., random neural events) in a given voxel or ROI. After physiological correction, the cleaned BOLD signal $y(t)$ at a given voxel or ROI is considered as the convolution of the voxel/ROI-specific HRF $h(t)$ and spontaneous neural events $x(t)$

$$y(t) = x(t) \otimes h(t) + c + \mathcal{E}(t)$$

where c is a constant term indicating the baseline magnitude of the BOLD response, $\mathcal{E}(t)$ is noise, and, $\otimes$ denotes convolution. Spontaneous point process events $\hat{n}(t)$ were identified as BOLD fluctuations of relatively large amplitude (one or more standard deviations away from the mean; see Figure 3a). Before identifying these events, we removed movement and physiological noise with the same set of 33 regressors as described above (see *MRI data preprocessing*). We then applied a high-pass filter (1/128Hz cut-off) and AR(1) serial autocorrelation corrections. These events were modeled as a train of Dirac delta functions given by

$$\hat{n}(t) = \sum_{r=0}^{\infty} \delta(\mathrm{t} - \tau)$$

where $\delta(\mathrm{t} - \tau)$ is the delta function. The ROI-specific HRF $h(t)$ was then fitted according to $\hat{n}(t)$ using a canonical HRF and two derivatives (temporal derivative and dispersion derivative; Friston et al., 2000). Once $h(t)$ was calculated, we obtained an approximation $\hat{n}(t)$ of the neural signal from the observed data using a Wiener filter. ROI-specific HRFs (Figure 3b) were estimated for all AAS nuclei (i.e., LC, VTA, SN, DR, MR, BF) and two validation regions (i.e., ACC, OCC) and one control region (i.e. pons). To maximize the number of spontaneous neural events, HRFs were estimated based on the concatenated BOLD signals from the two sessions (see Figure 3c for number

of detected pseudo-events per ROI). These HRFs were then convolved with the two pupil time series (i.e., pupil size [Figure 3e] and pupil derivative [Figure 3f]), forming the final pupil regressors that were entered into the GLMs for this analysis. GLMs were made up of a single pupil regressor-of-interest in addition to our physiological noise correction model described above. Analysis for pupil size included nine GLMs per participant, dedicated to six AAS nuclei (LC, VTA, SN, DR, MR, BF) and the three validation and control regions (ACC, OCC, pons). Similarly, nine models formed the analysis for the pupil derivative.

Systematic adjustment of HRF time-to-peak

To explore other possible temporal relationships between pupil size and AAS BOLD patterns, we carried out a second analysis of pupil-AAS coupling where the TTP of the HRF was systematically shifted in time (*time-to-peak [TTP] analysis*; Pais-Roldán et al., 2020). This was done using the canonical HRF (Friston et al., 2000), which by default has a TTP (delay of response relative to onset) of 6 s. To explore pupil-AAS coupling at shorter lags, we compared six HRFs with TTPs varying between 1, 2, 3, 4, 5, and 6 s. These HRFs were created using spm_hrf() in SPM, where parameter *p(1)* which refers to 'delay of response (relative to onset)' was adjusted from 6 (default) to 1, 2, 3, 4, and 5 respectively. Note that the 6-s TTP corresponds to the TTP used in the analysis corresponding to Schneider et al. (2016). These six HRFs were then convolved with the two pupil time series (pupil size, pupil derivative) for each participant, resulting in 12 pupil regressors. Each pupil size regressor was then added to the physiological noise correction model, making up six GLMs per participant, each focusing on one TTP (i.e., 1 s, 2 s, 3 s, 4 s, 5 s, 6 s). Similarly, six GLMs were created for the pupil derivative.

Analyses using unconvolved pupil time series

To further characterize the nature of pupil-AAS coupling we carried out two analyses using the *unconvolved* pupil time series. Firstly, we performed a cross-correlation analysis (Pais-Roldán et al., 2020) in which the preprocessed (downsampled, demeaned, unconvolved) pupil timeseries (size and derivative) were shifted forwards and backwards relative to the BOLD signal (denoised using the movement and physiological noise correction model and demeaned). Note that the BOLD signal from each ROI was first averaged and then entered into the cross-correlation analysis. This analysis is similar to the TTP analysis but used unconvolved pupil time series and allowed us to investigate both positive and negative lags between the pupil and BOLD signals, which was not possible with the TTP method. Secondly, in order to determine which frequencies were driving the observed pupil-BOLD cross-correlations, we estimated for each ROI the cross spectral power density (Yellin et al., 2015), the Fourier transform of the cross-correlations. We did this using cspd() in Matlab, setting the window length to 10 samples with an overlap of 3 samples.

Statistical analyses

All first-level GLMs described above were constructed in SPM12 with session (session 1, session 2) as a within-subject factor (n=56). For participants in which only one session could be included (i.e., due to pupil quality exclusion criteria or technical issues in a scanning session), a GLM was constructed using only one session (n = 14).

Second-level analyses were carried out by extracting *t*-values from single-subject contrast maps generated from the first-level analyses. These weights were then submitted to a second-level random effects analysis (one-sample *t*-test) in R using 'stats' package. To correct for multiple comparisons, alpha levels (set at 0.05) were adjusted by controlling the false discovery rate (FDR).

For the comparison analyses with Schneider et al. (2016) and Murphy et al. (2014), single-subject contrast maps obtained from first-level analyses were entered into second-level random effects analyses (one-sample t-test for Schneider et al. [2016] and a one-way repeated-measures analysis of variance [ANOVA] with three levels for Murphy et al. [2014]) in SPM12. Here, we used a cluster-forming voxel-level threshold of $p < .001$ (uncorrected). Alpha was set at 0.05 whole-brain family-wise error (FWE) corrected at the cluster level using Gaussian random field theory-based methods as implemented in SPM12 (Friston et al., 1996).

Data and code availability statement

Analyses code can be found here: https://github.com/bethlloyd/rs-fMRI_brainstem. Brain maps and processed pupil time series data will be uploaded to https://osf.io/9fkzp/ upon publication.

Declarations of interest

Authors declare that they have no conflict of interest.

Credit authorship and contribution statement

Beth Lloyd: Conceptualization, Methodology, Software, Validation, Formal analysis, Investigation, Data Curation, Writing – Original Draft, Visualization. **Lycia D. de Voogd:** Conceptualization, Methodology, Software, Investigation, Data Curation, Writing – Review & Editing. **Verónica Mäki-Marttunen:** Conceptualization, Methodology , Supervision, Writing – Review & Editing. **Sander Nieuwenhuis:** Conceptualization, Methodology, Resources, Writing – Review & Editing, Supervision, Funding acquisition.

Acknowledgements

Data collection was funded by the Templeton World Charity Foundation, Inc. network "Survival Circuits Influences on Human Nature" to LdV, Elizabeth Phelps and Joseph LeDoux. This publication is part of a Vici project

(with project number VI.C.181.032) that is financed by the Dutch Research Council (NWO) awarded to Sander Nieuwenhuis. We would also like to thank Birte Forstmann and Steven Miletić for their helpful contributions.

References

Alkemade, A., Mulder, M. J., Groot, J. M., Isaacs, B. R., Van, N., Lute, N., Js, S., Bazin, P., & Forstmann, B. U. (2020). NeuroImage The A msterdam Ultra- h igh fi e ld a dult lifespan d atabase (AHEAD): A freely available multimodal 7 Tesla submillimeter magnetic resonance imaging database. *NeuroImage*, *221*(July), 117200. https://doi.org/10.1016/j.neuroimage.2020.117200

Beliveau, V., Svarer, C., Frokjaer, V. G., Knudsen, G. M., Greve, D. N., & Fisher, P. M. (2015). Functional connectivity of the dorsal and median raphe nuclei at rest. *NeuroImage*. https://doi.org/10.1016/j.neuroimage.2015.04.065

Birn, R. M., Diamond, J. B., Smith, M. A., & Bandettini, P. A. (2006). Separating respiratory-variation-related fluctuations from neuronal-activity-related fluctuations in fMRI. *NeuroImage*, *31*(4), 1536–1548. https://doi.org/10.1016/j.neuroimage.2006.02.048

Breeden, A. L., Siegle, G. J., Norr, M. E., Gordon, E. M., & Vaidya, C. J. (2016). *Coupling between spontaneous pupillary fluctuations and brain activity relates to inattentiveness*. 1–7. https://doi.org/10.1111/ejn.13424

Breton-provencher, V., & Sur, M. (2019). Active control of arousal by a locus coeruleus GABAergic circuit. *Nature Neuroscience*, *22*(February). https://doi.org/10.1038/s41593-018-0305-z

Brooks, J. C. W., Faull, O. K., Pattinson, K. T. S., & Jenkinson, M. (2013). Physiological noise in brainstem fMRI. *Frontiers in Human Neuroscience*, *c*(OCT), 1–13. https://doi.org/10.3389/fnhum.2013.00623

Bunzeck, N., & Düzel, E. (2006). Absolute Coding of Stimulus Novelty in the Human Substantia Nigra/VTA. *Neuron*. https://doi.org/10.1016/j.neuron.2006.06.021

Cazettes, F., Reato, D., Morais, J. P., Renart, A., & Mainen, Z. F. (2021). Phasic Activation of Dorsal Raphe Serotonergic Neurons Increases Pupil Size. *Current Biology*. https://doi.org/10.1016/j.cub.2020.09.090

Cazettes, F., Reato, D., Morais, P., Renart, A., Mainen, Z. F., Morais, P., Renart, A., & Mainen, Z. F. (2021). *Report Phasic Activation of Dorsal Raphe Serotonergic Neurons Increases Pupil Size ll ll Phasic Activation of Dorsal Raphe Serotonergic Neurons Increases Pupil Size*. 192–197. https://doi.org/10.1016/j.cub.2020.09.090

Clewett, D. V., Lee, T. H., Greening, S., Ponzio, A., Margalit, E., & Mather, M. (2016). Neuromelanin marks the spot: identifying a locus coeruleus biomarker of cognitive reserve in healthy aging. *Neurobiology of Aging*, *37*, 117–126. https://doi.org/10.1016/j.neurobiolaging.2015.09.019

Colizoli, O., Gee, J. W. De, van der Zwaag, W., & Donner, T. H. (2022). Functional magnetic resonance imaging

responses during perceptual decision-making at 3 and 7 T in human cortex , striatum , and brainstem. *Human Brain Mapping*, *43*(4), 1265–1279. https://doi.org/10.1002/hbm.25719

de Gee, J. W., Colizoli, O., Kloosterman, N. A., Knapen, T., Nieuwenhuis, S., & Donner, T. H. (2017). Dynamic modulation of decision biases by brainstem arousal systems. *ELife*. https://doi.org/10.7554/eLife.23232

DiNuzzo, M., Mascali, D., Moraschi, M., Bussu, G., Maugeri, L., Mangini, F., Fratini, M., & Giove, F. (2019). Brain Networks Underlying Eye's Pupil Dynamics. *Frontiers in Neuroscience*. https://doi.org/10.3389/fnins.2019.00965

Drew, P. J., Mateo, C., Turner, K. L., Yu, X., & Kleinfeld, D. (2020). Perspective Ultra-slow Oscillations in fMRI and Resting-State Connectivity : Neuronal and Vascular Contributions and Technical Confounds. *Neuron*, *107*(5), 782–804. https://doi.org/10.1016/j.neuron.2020.07.020

Eickhoff, S. B., Stephan, K. E., Mohlberg, H., Grefkes, C., Fink, G. R., Amunts, K., & Zilles, K. (2005). A new SPM toolbox for combining probabilistic cytoarchitectonic maps and functional imaging data. *NeuroImage*. https://doi.org/10.1016/j.neuroimage.2004.12.034

Ewert, S., Horn, A., Finkel, F., Li, N., Kühn, A. A., & Herrington, T. M. (2019). Optimization and comparative evaluation of nonlinear deformation algorithms for atlas-based segmentation of DBS target nuclei. *NeuroImage*. https://doi.org/10.1016/j.neuroimage.2018.09.061

Forstmann, B. U., De Hollander, G., Van Maanen, L., Alkemade, A., & Keuken, M. C. (2017). Towards a mechanistic understanding of the human subcortex. *Nature Reviews Neuroscience*, *18*(1), 57–65. https://doi.org/10.1038/nrn.2016.163

Friston, K. J., Holmes, A., Poline, J. B., Price, C. J., & Frith, C. D. (1996). Detecting activations in pet and fMRI: Levels of inference and power. *NeuroImage*. https://doi.org/10.1006/nimg.1996.0074

Friston, K. J., Mechelli, A., Turner, R., & Price, C. J. (2000). Nonlinear responses in fMRI: The balloon model, Volterra kernels, and other hemodynamics. *NeuroImage*. https://doi.org/10.1006/nimg.2000.0630

Glover, G. H., Li, T. Q., & Ress, D. (2000). Image-based method for retrospective correction of physiological motion effects in fMRI: RETROICOR. *Magnetic Resonance in Medicine*. https://doi.org/10.1002/1522-2594(200007)44:1<162::AID-MRM23>3.0.CO;2-E

Handwerker, D. A., Ollinger, J. M., & D'Esposito, M. (2004). Variation of BOLD hemodynamic responses across subjects and brain regions and their effects on statistical analyses. *NeuroImage*. https://doi.org/10.1016/j.neuroimage.2003.11.029

Harvey, A. K., Pattinson, K. T. S., Brooks, J. C. W., Mayhew, S. D., Jenkinson, M., & Wise, R. G. (2008). Brainstem functional magnetic resonance imaging: Disentangling signal from physiological noise. *Journal of Magnetic Resonance Imaging*. https://doi.org/10.1002/jmri.21623

Joshi, S., & Gold, J. I. (2020). Pupil Size as a Window on Neural Substrates of Cognition. In *Trends in Cognitive*

Sciences. https://doi.org/10.1016/j.tics.2020.03.005

Joshi, S., Li, Y., Kalwani, R. M., & Gold, J. I. (2016). Relationships between Pupil Diameter and Neuronal Activity in the Locus Coeruleus, Colliculi, and Cingulate Cortex. *Neuron*. https://doi.org/10.1016/j.neuron.2015.11.028

Keren, N. I., Lozar, C. T., Harris, K. C., Morgan, P. S., & Eckert, M. A. (2009). In vivo mapping of the human locus coeruleus. *NeuroImage*. https://doi.org/10.1016/j.neuroimage.2009.06.012

Keren, N. I., Taheri, S., Vazey, E. M., Morgan, P. S., Granholm, A. C. E., Aston-Jones, G. S., & Eckert, M. A. (2015). Histologic validation of locus coeruleus MRI contrast in post-mortem tissue. *NeuroImage*, *113*, 235–245. https://doi.org/10.1016/j.neuroimage.2015.03.020

Krause, F., Benjamins, C., Eck, J., Lührs, M., van Hoof, R., & Goebel, R. (2019). Active head motion reduction in magnetic resonance imaging using tactile feedback. *Human Brain Mapping*, *40*(14), 4026–4037. https://doi.org/10.1002/hbm.24683

Lau, C., Zhou, I. Y., Cheung, M. M., Chan, K. C., & Wu, E. X. (2011). BOLD temporal dynamics of rat superior colliculus and lateral geniculate nucleus following short duration visual stimulation. *PLoS ONE*. https://doi.org/10.1371/journal.pone.0018914

Lewis, L. D., Setsompop, K., Rosen, B. R., & Polimeni, J. R. (2018). Stimulus-dependent hemodynamic response timing across the human subcortical-cortical visual pathway identified through high spatiotemporal resolution 7T fMRI. *NeuroImage*. https://doi.org/10.1016/j.neuroimage.2018.06.056

Liu, K. Y., Marijatta, F., Hämmerer, D., Acosta-Cabronero, J., Düzel, E., & Howard, R. J. (2017a). Magnetic resonance imaging of the human locus coeruleus: A systematic review. *Neuroscience and Biobehavioral Reviews*, *83*(September), 325–355. https://doi.org/10.1016/j.neubiorev.2017.10.023

Liu, K. Y., Marijatta, F., Hämmerer, D., Acosta-Cabronero, J., Düzel, E., & Howard, R. J. (2017b). Magnetic resonance imaging of the human locus coeruleus: A systematic review. *Neuroscience and Biobehavioral Reviews*, *83*(June), 325–355. https://doi.org/10.1016/j.neubiorev.2017.10.023

Mäki-Marttunen, V., & Espeseth, T. (2021). Uncovering the locus coeruleus: Comparison of localization methods for functional analysis. *NeuroImage*. https://doi.org/10.1016/j.neuroimage.2020.117409

Mateo, C., Knutsen, P. M., Tsai, P. S., & Shih, A. Y. (2017). Entrainment of Arteriole Vasomotor Fluctuations by Neural Activity Is a Basis of Blood-Oxygenation- Article Entrainment of Arteriole Vasomotor Fluctuations by Neural Activity Is a Basis of Blood-Oxygenation-. *Neuron*, *96*(4), 936-948.e3. https://doi.org/10.1016/j.neuron.2017.10.012

Mather, M., Joo Yoo, H., Clewett, D. V., Lee, T. H., Greening, S. G., Ponzio, A., Min, J., & Thayer, J. F. (2017). Higher locus coeruleus MRI contrast is associated with lower parasympathetic influence over heart rate variability. *NeuroImage*, *150*(November 2016), 329–335.

https://doi.org/10.1016/j.neuroimage.2017.02.025

Matt, E., Fischmeister, F. P. S., Amini, A., Robinson, S. D., Weber, A., Foki, T., Gizewski, E. R., & Beisteiner, R. (2019). Improving sensitivity, specificity, and reproducibility of individual brainstem activation. *Brain Structure and Function*, *224*(8), 2823–2838. https://doi.org/10.1007/s00429-019-01936-3

Megemont, M., & Mcburney-, J. (2022). Pupil diameter is not an accurate real- - time readout of locus coeruleus activity. *ELife*, *11*, e70510.

Miletić, S., Bazin, P. L., Weiskopf, N., van der Zwaag, W., Forstmann, B. U., & Trampel, R. (2020). fMRI protocol optimization for simultaneously studying small subcortical and cortical areas at 7 T. *NeuroImage*, *219*(December 2019). https://doi.org/10.1016/j.neuroimage.2020.116992

Murphy, P. R., O'Connell, R. G., O'Sullivan, M., Robertson, I. H., & Balsters, J. H. (2014). Pupil diameter covaries with BOLD activity in human locus coeruleus. *Human Brain Mapping*. https://doi.org/10.1002/hbm.22466

Pais-Roldán, P., Takahashi, K., Sobczak, F., Chen, Y., Zhao, X., Zeng, H., Jiang, Y., & Yu, X. (2020). Indexing brain state-dependent pupil dynamics with simultaneous fMRI and optical fiber calcium recording. *Proceedings of the National Academy of Sciences of the United States of America*. https://doi.org/10.1073/pnas.1909937117

Pfeffer, T., Keitel, C., Kluger, D. S., Keitel, A., Russmann, A., Thut, G., Donner, T. H., & Gross, J. (2022). Coupling of pupil-and neuronal population dynamics reveals diverse influences of arousal on cortical processing. *ELife*, *11*, 1–28. https://doi.org/10.7554/ELIFE.71890

Poser, B. A., Versluis, M. J., Hoogduin, J. M., & Norris, D. G. (2006). BOLD contrast sensitivity enhancement and artifact reduction with multiecho EPI: Parallel-acquired inhomogeneity-desensitized fMRI. *Magnetic Resonance in Medicine*, *55*(6), 1227–1235. https://doi.org/10.1002/mrm.20900

Priovoulos, N., Jacobs, H. I. L., Ivanov, D., Uludağ, K., Verhey, F. R. J., & Poser, B. A. (2018). High-resolution in vivo imaging of human locus coeruleus by magnetization transfer MRI at 3T and 7T. *NeuroImage*. https://doi.org/10.1016/j.neuroimage.2017.07.045

Puckett, A. M., Bollmann, S., Poser, B. A., Palmer, J., Barth, M., & Cunnington, R. (2018). NeuroImage Using multi-echo simultaneous multi-slice (SMS) EPI to improve functional MRI of the subcortical nuclei of the basal ganglia at ultra-high fi eld (7T). *NeuroImage*, *172*(December 2017), 886–895. https://doi.org/10.1016/j.neuroimage.2017.12.005

Rangaprakash, D., Wu, G. R., Marinazzo, D., Hu, X., & Deshpande, G. (2018). Hemodynamic response function (HRF) variability confounds resting-state fMRI functional connectivity. *Magnetic Resonance in Medicine*. https://doi.org/10.1002/mrm.27146

Reimer, J., McGinley, M. J., Liu, Y., Rodenkirch, C., Wang, Q., McCormick, D. A., & Tolias, A. S. (2016). Pupil fluctuations track rapid changes in adrenergic and cholinergic activity in cortex. *Nature Communications*.

https://doi.org/10.1038/ncomms13289

Schneider, M., Hathway, P., Leuchs, L., Sämann, P. G., Czisch, M., & Spoormaker, V. I. (2016). Spontaneous pupil dilations during the resting state are associated with activation of the salience network. *NeuroImage*. https://doi.org/10.1016/j.neuroimage.2016.06.011

Shine, J. M., Müller, E. J., Munn, B., Cabral, J., Moran, R. J., & Breakspear, M. (2021). Computational models link cellular mechanisms of neuromodulation to large-scale neural dynamics. In *Nature Neuroscience*. https://doi.org/10.1038/s41593-021-00824-6

Singh, K., Cauzzo, S., García-gomar, M. G., Stauder, M., Vanello, N., Passino, C., & Bianciardi, M. (2022). *NeuroImage Functional connectome of arousal and motor brainstem nuclei in living humans by 7 Tesla resting-state fMRI*. *249*(November 2021). https://doi.org/10.1016/j.neuroimage.2021.118865

Thiele, A., & Bellgrove, M. A. (2018). Neuromodulation of Attention. In *Neuron*. https://doi.org/10.1016/j.neuron.2018.01.008

Trutti, A. C., Fontanesi, L., Mulder, M. J., Bazin, P. L., Hommel, B., & Forstmann, B. U. (2021). A probabilistic atlas of the human ventral tegmental area (VTA) based on 7 Tesla MRI data. *Brain Structure and Function*. https://doi.org/10.1007/s00429-021-02231-w

Turker, H. B., Riley, E., Luh, W. M., Colcombe, S. J., & Swallow, K. M. (2021). Estimates of locus coeruleus function with functional magnetic resonance imaging are influenced by localization approaches and the use of multi-echo data. *NeuroImage*. https://doi.org/10.1016/j.neuroimage.2021.118047

Tzourio-Mazoyer, N., Landeau, B., Papathanassiou, D., Crivello, F., Etard, O., Delcroix, N., Mazoyer, B., & Joliot, M. (2002). Automated anatomical labeling of activations in SPM using a macroscopic anatomical parcellation of the MNI MRI single-subject brain. *NeuroImage*, *15*(1), 273–289. https://doi.org/10.1006/nimg.2001.0978

Van Buuren, M., Gladwin, T. E., Zandbelt, B. B., Van Den Heuvel, M., Ramsey, N. F., Kahn, R. S., & Vink, M. (2009). Cardiorespiratory effects on default-mode network activity as measured with fMRI. *Human Brain Mapping*, *30*(9), 3031–3042. https://doi.org/10.1002/hbm.20729

Van den Brink, R., Colizoli, O., de Gee, J. W., Donner, T. H., (2019/11). Neuromodulatory brainstem activity predicts intrinsic co-fluctuations in cortical activity. *Society for Neuroscience.*

Varazzani, C., San-Galli, A., Gilardeau, S., & Bouret, S. (2015). Noradrenaline and dopamine neurons in the reward/effort trade-off: A direct electrophysiological comparison in behaving monkeys. *Journal of Neuroscience*. https://doi.org/10.1523/JNEUROSCI.0454-15.2015

Wall, M. B., Walker, R., & Smith, A. T. (2009). Functional imaging of the human superior colliculus: An optimised approach. *NeuroImage*. https://doi.org/10.1016/j.neuroimage.2009.05.094

Wu, G. R., Colenbier, N., Van Den Bossche, S., Clauw, K., Johri, A., Tandon, M., & Marinazzo, D. (2021). rsHRF: A

toolbox for resting-state HRF estimation and deconvolution. *NeuroImage*, *244*(June). https://doi.org/10.1016/j.neuroimage.2021.118591

Wu, G. R., Liao, W., Stramaglia, S., Ding, J. R., Chen, H., & Marinazzo, D. (2013). A blind deconvolution approach to recover effective connectivity brain networks from resting state fMRI data. *Medical Image Analysis*. https://doi.org/10.1016/j.media.2013.01.003

Yang, H., Bari, B. A., Cohen, J. Y., & O'Connor, D. H. (2021). Locus coeruleus spiking differently correlates with s1 cortex activity and pupil diameter in a tactile detection task. *ELife*. https://doi.org/10.7554/eLife.64327

Yellin, D., Berkovich-ohana, A., & Malach, R. (2015). NeuroImage Coupling between pupil fl uctuations and resting-state fMRI uncovers a slow build-up of antagonistic responses in the human cortex. *NeuroImage*, *106*, 414–427. https://doi.org/10.1016/j.neuroimage.2014.11.034

Yen, C. C. C., Fukuda, M., & Kim, S. G. (2011). BOLD responses to different temporal frequency stimuli in the lateral geniculate nucleus and visual cortex: Insights into the neural basis of fMRI. *NeuroImage*. https://doi.org/10.1016/j.neuroimage.2011.06.022

Yi, Y.-J., Lüsebrink, F., Maaß, A., Ziegler, G., Yakupov, R., Kreißl, M. C., Betts, M., Speck, O., Düzel, E., & Hämmerer, D. (2021). It is the Locus Coeruleus! Or… is it? : A proposition for analyses and reporting standards for structural and functional magnetic resonance imaging of the noradrenergic Locus Coeruleus. *BioRxiv*, 2021.10.01.462807. https://doi.org/10.1101/2021.10.01.462807

Yushkevich, P. A., Piven, J., Hazlett, H. C., Smith, R. G., Ho, S., Gee, J. C., & Gerig, G. (2006). User-guided 3D active contour segmentation of anatomical structures: Significantly improved efficiency and reliability. *NeuroImage*, *31*(3), 1116–1128. https://doi.org/10.1016/j.neuroimage.2006.01.015

Zaborszky, L., Hoemke, L., Mohlberg, H., Schleicher, A., Amunts, K., & Zilles, K. (2008). Stereotaxic probabilistic maps of the magnocellular cell groups in human basal forebrain. *NeuroImage*, *42*(3), 1127–1141. https://doi.org/10.1016/j.neuroimage.2008.05.055